

# Supplementary information

*for*

## Quantifying the influence of channel sinuosity on the depositional mechanics of channelized turbidity currents: A laboratory study

Kyle M. Straub<sup>a</sup>, David Mohrig<sup>b</sup>, James Buttles<sup>b</sup>, Brandon McElroy<sup>b</sup>, and Carlos Pirmez<sup>c</sup>

<sup>a</sup>Department of Earth and Environmental Sciences, Tulane University, New Orleans, LA 70118, U.S.A.

<sup>b</sup>Department of Geological Sciences, The University of Texas at Austin, Austin, TX 78712, U.S.A.

<sup>c</sup>Shell International Exploration and Production, Inc., P.O. Box 481, Houston, TX 77001, U.S.A.

### Contents

<b>1</b>	<b>Supplemental video legends</b>	<b>S2</b>
<b>2</b>	<b>Scaling of experiments</b>	<b>S3</b>
<b>3</b>	<b>ADV velocity measurements &amp; confirmation of shear flows</b>	<b>S11</b>
<b>4</b>	<b>PCADP velocity measurements and entrainment</b>	<b>S13</b>
	<b>References</b>	<b>S15</b>

## **DIGITAL VIDEOS**

Supplemental Video 1. Video of laboratory experiments documenting interactions between turbidity currents and topography in aggrading straight, low sinuosity, and high sinuosity submarine channels. Digital video was collected from camera positioned directly above experimental basin and therefore yield a close to synoptic representation of the channelized-overbank flow field. Video is presented at 4 times the actual experimental time. Video includes: 1) experimental straight channel flows 2, 6, and 11, 2) experimental low sinuosity channel flows 1, 5, 8, 15, 20, 25, and 32, and 3) experimental high sinuosity channel flows 2, 8, 15, and 20. Each flow is clipped to incorporate the passage of both the turbidity current head and a dye injection.

## SCALING

Our experiments were conducted at a reduced scale relative to submarine channels. It is therefore important to discuss how our model systems compare to the natural environment. This comparison has three components: 1) a simple geometric scaling of the relatively static channel topography; 2) a dynamic scaling of flow properties for estimating equivalence between model and natural flows; and 3) a dynamic scaling of the sediment transport in order to roughly compare particle sizes being moved by the model and natural flows. The scaling is only intended to guide how experimental results might be applied to the interpretation of natural channels. Our experiments were not designed to simulate environmental conditions associated with a specific system but rather were carried out to better understand the depositional consequences of interactions between turbidity currents and channels.

The geometric scaling for our experiment was chosen to be 1/1000. Maximum width and depth for the straight and high sinuosity laboratory channels therefore correspond to natural scales of 400 m and 110 m and 515 m and 80 m for the low sinuosity channel. Bend amplitude and wavelength for the high sinuosity channel correspond to natural scales of 390 m and 2.25 km and for the low sinuosity channel these correspond to 285 m and 2.51 km respectively. The wavelength/amplitude ratio was 5.8 in the high sinuosity channel and 8.8 in the low sinuosity channel. These values compare favorably with measurements from natural channels assembled by Pirmez and Imran (2003): wavelength/amplitude ranges between 0.4 and 8.0.

The comparison between properties of the experimental and natural or prototype flows focuses on the densimetric Froude number ( $Fr = \bar{u} / \sqrt{[(\rho_c / \rho_a) - 1]gH}$ ) and Reynolds number ( $Re = \bar{u}H / \nu$ ),

where  $\bar{u}$  is depth averaged velocity,  $\rho_c$  is current density,  $\rho_a$  is the ambient fluid density,  $g$  is gravitational acceleration,  $H$  is current thickness, and  $\nu$  is kinematic viscosity. An approximate dynamic similarity between the model and a natural system is ensured by setting  $Fr_{(model)} = Fr_{(prototype)}$  (Graf, 1971). Assuming a similar excess density for the experimental and natural currents, equality in densimetric Froude number is satisfied by prototype values for  $\bar{u}$  and  $H$  of 2.5 m/s and 110 m for the high sinuous channel experiments, 3.2 m/s and 80 m for the low sinuosity channel and 4.1 m/s and 110 m for the straight channel. Equality in densimetric Froude number also constrains the duration of a comparable natural current ( $T$ ) to be 2.7 hr for the straight and high sinuosity channels and 2.1 hr for the low sinuosity channel. Reynolds numbers for the model and prototype cannot be matched. The characteristic Reynolds number for model currents were  $8.2 \times 10^3$ ,  $1.2 \times 10^4$ , and  $1.4 \times 10^4$  for the high sinuosity, low sinuosity, and straight channel experiments respectively. The characteristic Reynolds number for a comparable natural current would be  $3.0 \times 10^8$ . Fortunately the model-current value was sufficiently large to ensure the approximate Reynolds similarity for fully turbulent gravity currents proposed by Parsons and García (1998).

Altinakar et al. (1996) have shown that the lower portion of velocity profiles for turbidity currents developing on a flat bed under approximately steady and uniform conditions exhibit a logarithmic form that can be described by

$$(2) \quad u(z) = \frac{u^*}{\kappa} \ln \left( \frac{z}{z_0} \right),$$

where  $u(z)$  is the time-averaged streamwise velocity as a function of elevation above the bed,  $z$ ,  $\kappa$  is von Kármán's constant and is equal to 0.4, and  $z_0$  is a roughness parameter, equal to the elevation at which the extrapolated logarithmic velocity profile goes to zero. We have estimated the characteristic shear velocity associated with the model currents,  $u^*_{model}$ , by fitting (2) to velocity data collected with the PCADP from 5 currents in the straight channel experiment, 5 currents in the low sinuosity channel

experiment, and 3 currents in the high sinuosity channel experiment. The fit to the portion of the velocity profiles situated between the bed and the velocity maximum is good, with the average  $R^2$  equal to 0.97, 0.92, and 0.88 for the high sinuosity, low sinuosity, and straight channel experiments respectively (Figure Supp. 1, 2, and 3). The regressions yielded  $u^*_{model}$  equal to  $2.0 \pm 0.6 \times 10^{-2}$  m/s,  $3.5 \pm 0.5 \times 10^{-2}$  m/s, and  $5.2 \pm 0.8 \times 10^{-2}$  m/s for the high sinuosity, low sinuosity, and straight channel experiments respectively. A characteristic friction coefficient,  $C_f$ , for the model currents can be calculated from this estimate for  $u^*_{model}$  and the measured  $\bar{u}_{model}$  using

$$(3) \quad u^* = \sqrt{C_f \bar{u}}$$

The resulting  $C_{f(model\_high\ sinuosity)} = 6.2 \times 10^{-2}$ ,  $C_{f(model\_low\ sinuosity)} = 7.2 \times 10^{-2}$ , and  $C_{f(model\_straight)} = 1.6 \times 10^{-1}$  are consistent with other laboratory measures of  $C_{f(model)}$  for turbidity currents reported by Parker et al. (1987) and Garcia (1994). A prototype shear velocity can be determined using (3) and the estimated values for  $\bar{u}_{prototype}$  and  $C_{f(prototype)}$ . We have reduced the prototype value for  $C_f$  by an order of magnitude to account for the weak dependence of bed friction coefficient with turbidity-current scale as summarized in Parker et al. (1987) and Garcia (1994). The calculated  $u^*_{prototype\_high\ sinuosity} = 2.0 \times 10^{-1}$  m/s, the calculated  $u^*_{prototype\_low\ sinuosity} = 3.5 \times 10^{-1}$  m/s, and the calculated  $u^*_{prototype\_straight} = 5.3 \times 10^{-1}$  m/s.

Grain sizes used in the experiment can be compared to natural channels by estimating equivalent sediment transporting conditions between the two systems. Since the predominant mode of transport is suspended load, we make the dynamic comparison by matching the ratio  $w_s / u^*$ . This scaling parameter was chosen because it best characterizes the degree to which particles of various sizes are suspended within the transporting current, with  $w_s$  serving as the scale value for downward particle advection and  $u^*$  being the scale value for the effective diffusion of particles into the interior flow by turbulent eddies. Particle settling velocities for D5, D10, D50, D90, and D95 equaled  $5.1 \times 10^{-5}$  m/s,  $1.3 \times 10^{-4}$  m/s,  $7.8 \times 10^{-4}$  m/s,  $2.0 \times 10^{-3}$  m/s, and  $2.7 \times 10^{-3}$  m/s, respectively in the straight, low sinuosity, and high sinuosity channels. Calculated experimental values for  $w_s / u^*_{(D5)}$ ,  $w_s / u^*_{(D10)}$ ,  $w_s / u^*_{(D50)}$ ,  $w_s / u^*_{(D90)}$ , and  $w_s / u^*_{(D95)}$  are  $2.5 \times 10^{-4}$ ,  $6.5 \times 10^{-3}$ ,  $3.9 \times 10^{-2}$ ,  $1.0 \times 10^{-1}$ , and  $1.3 \times 10^{-1}$  in the high sinuosity channel. Calculated experimental values for  $w_s / u^*_{(D5)}$ ,  $w_s / u^*_{(D10)}$ ,  $w_s / u^*_{(D50)}$ ,  $w_s / u^*_{(D90)}$ , and  $w_s / u^*_{(D95)}$  are  $1.5 \times 10^{-3}$ ,  $3.7 \times 10^{-3}$ ,  $2.2 \times 10^{-2}$ ,  $5.7 \times 10^{-2}$ , and  $7.7 \times 10^{-2}$  in the low sinuosity channel. Calculated experimental values for  $w_s / u^*_{(D5)}$ ,  $w_s / u^*_{(D10)}$ ,  $w_s / u^*_{(D50)}$ ,  $w_s / u^*_{(D90)}$ , and  $w_s / u^*_{(D95)}$  are  $9.8 \times 10^{-4}$ ,  $2.5 \times 10^{-3}$ ,  $1.5 \times 10^{-2}$ ,  $3.8 \times 10^{-2}$ , and  $5.2 \times 10^{-1}$  in the straight channel. All of these values are much less than 1, the minimum value for significant suspension transport originally reported by Bagnold (1966). By satisfying the equality  $w_s / u^*_{(model)} = w_s / u^*_{(prototype)}$  we estimate that D5, D10, D50, D90, and D95 for the experimental flows in the high sinuosity channel correspond to particle sizes of 25  $\mu\text{m}$ , 40  $\mu\text{m}$ , 110  $\mu\text{m}$ , 203  $\mu\text{m}$ , and 251  $\mu\text{m}$  for flows at natural scale and that D5, D10, D50, D90, and D95, for the experimental flows in the low sinuosity channel correspond to particle sizes of 26  $\mu\text{m}$ , 40  $\mu\text{m}$ , 111  $\mu\text{m}$ , 203  $\mu\text{m}$ , and 252  $\mu\text{m}$ , for the experimental flows in the straight channel correspond to particle sizes of 25  $\mu\text{m}$ , 40  $\mu\text{m}$ , 111  $\mu\text{m}$ , 205  $\mu\text{m}$ , and 255  $\mu\text{m}$  for flows at natural scale (Table Suppl. 1).

The above sediment-transport scaling is directed at estimating properties associated with the interiors of currents. We are also interested in assessing near-bed conditions using the particle Reynolds number,  $Re_s = u^* D / \nu$ . The appropriate model and prototype values for  $u^*$  and D95, as well as  $\nu = 1.0 \times 10^{-6}$  m<sup>2</sup>/s yield estimates for  $Re_{s(model\_high\ sinuosity)}$ ,  $Re_{s(prototype\_high\ sinuosity)}$ ,  $Re_{s(model\_low\ sinuosity)}$ ,  $Re_{s(prototype\_low\ sinuosity)}$ ,  $Re_{s(model\_straight)}$  and  $Re_{s(prototype\_straight)}$  of 1.2, 50, 2.0, 86.0, 3.1 and 135. For the case of a flat bed the experimental system has a hydraulically smooth boundary and the natural system has a hydraulically transitional boundary, implying that scale of particles composing the beds is smaller than (model) or comparable to (prototype) the thickness of the viscous sublayer (Graf, 1971). In both cases viscous effects are important in setting the style of the near-bed sediment-transport conditions. Nino et al. (2003) performed a set of experiments to determine threshold conditions for the entrainment of bed

sediment into suspension for cases of small  $R_p$  where viscous effects are significant.  $R_p$  is a dimensionless particle diameter defined as:

$$(4) \quad R_p = \frac{\sqrt{RgD^3}}{\nu}$$

where  $R$  is the submerged specific density for particles of representative diameter  $D$  in a fluid with a kinematic viscosity of  $\nu$ . These threshold conditions for particle entrainment into suspension are plotted in Figure Supp 3 as functions of  $R_p$  and  $u^*/w_s$  using the function presented in Nino et al., (2003):

$$(5) \quad \frac{u^*}{w_s} = 21.2R_p^{-1.2}$$

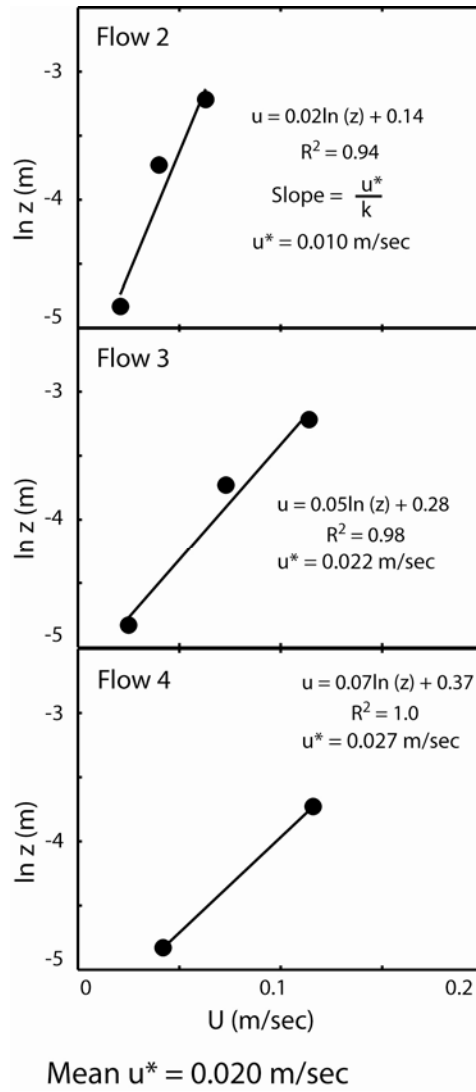
Estimated values for  $R_p$  and  $u^*/w_s$  for our experiment are also plotted in Figure Supp. 4. These values indicate that experimental conditions associated with our model lie within or very close to the suspension regime as measured and predicted by Nino et. al (2003).

Supplemental Figure 1. Estimation of  $u^*$  for high sinuosity channel experiment obtained with best-fit slope of  $\ln z$  vs. current velocity plots. Velocity measurements were obtained below the velocity maximum of each sample profile. Mean  $u^*$  value of the 3 flow events presented equaled 0.020 m/sec.

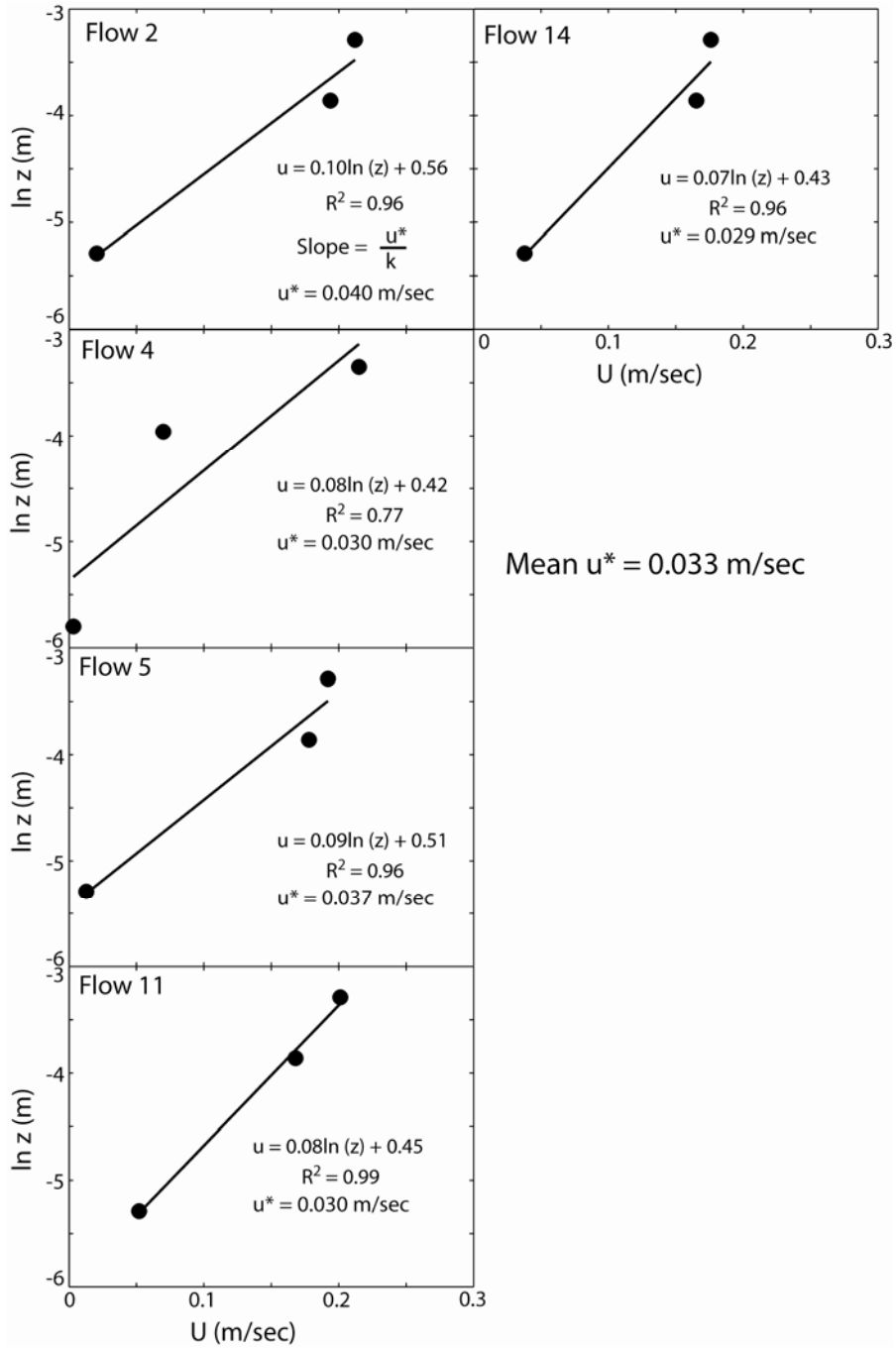
Supplemental Figure 2. Estimation of  $u^*$  for low sinuosity channel experiment obtained with best-fit slope of  $\ln z$  vs. current velocity plots. Velocity measurements were obtained below the velocity maximum of each sample profile. Mean  $u^*$  value of the 5 flow events presented equaled 0.035 m/sec.

Supplemental Figure 3. Estimation of  $u^*$  for straight channel experiment obtained with best-fit slope of  $\ln z$  vs. current velocity plots. Velocity measurements were obtained below the velocity maximum of each sample profile. Mean  $u^*$  value of the 3 flow events presented equaled 0.052 m/sec.

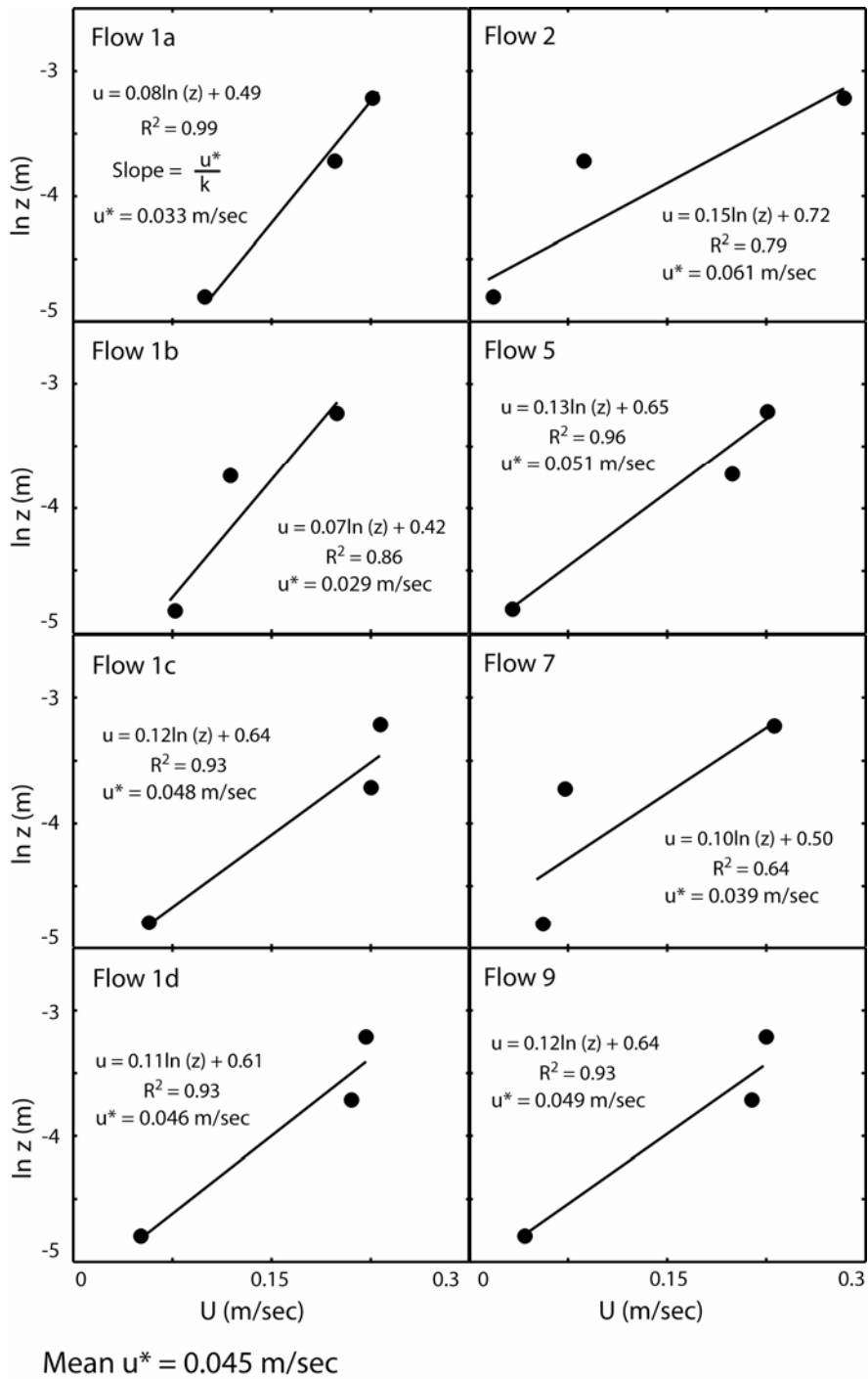
Supplemental Figure 4. Comparison of experimental conditions in this study to threshold of particle entrainment into suspension conditions reported by Nino et al.(Nino et al., 2003). Gray dashed line represents experimental conditions in the high sinuosity channel study defined between D5 and D95 particle sizes of deposit at channel axis at apex of bend 2. Red dashed line represents experimental conditions in the low sinuosity channel study defined between D5 and D95 particle sizes of deposit at channel axis at apex of bend 2. Blue dashed line represents experimental conditions in straight channel study defined between D5 and D95 particle sizes of deposit at channel axis at 1.8 m from channel entrance.



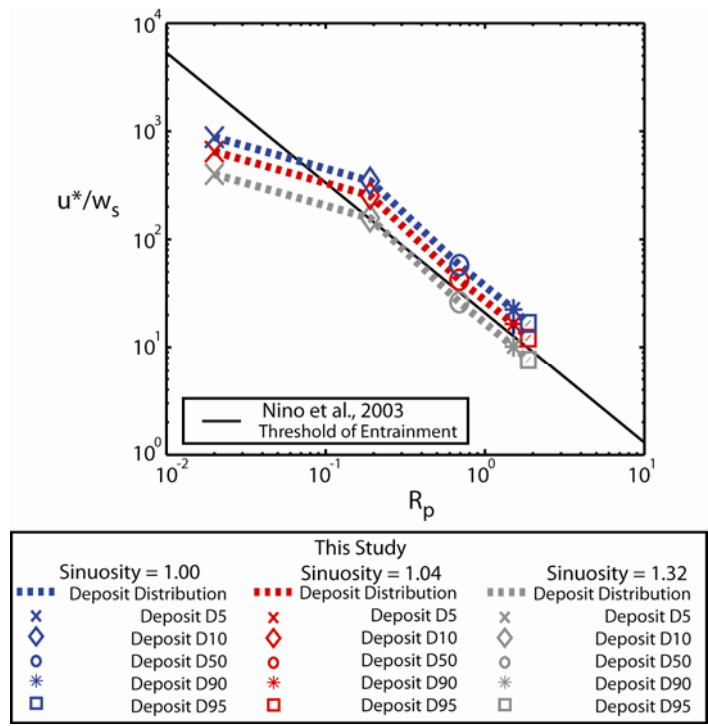
**Supplemental Figure 1**



**Supplemental Figure 2**



Supplemental Figure 3



**Supplemental Figure 4**

	Particle diameter ( $\mu\text{m}$ ) model	$w_j$ (m/s)	$w_j/u^*$ high sinuosity	$w_j/u^*$ low sinuosity	$w_j/u^*$ straight	Particle diameter ( $\mu\text{m}$ ) prototype high sinuosity	Particle diameter ( $\mu\text{m}$ ) prototype low sinuosity	Particle diameter ( $\mu\text{m}$ ) prototype straight
D5	3.1	$5.1 \times 10^{-5}$	$2.5 \times 10^{-4}$	$1.5 \times 10^{-3}$	$9.8 \times 10^{-4}$	25	26	25
D10	12.9	$1.3 \times 10^{-4}$	$6.5 \times 10^{-3}$	$3.7 \times 10^{-3}$	$2.5 \times 10^{-3}$	40	40	40
D50	31	$7.8 \times 10^{-4}$	$3.9 \times 10^{-2}$	$2.2 \times 10^{-2}$	$1.5 \times 10^{-2}$	110	111	111
D90	52	$2.0 \times 10^{-3}$	$1.0 \times 10^{-1}$	$5.7 \times 10^{-2}$	$3.8 \times 10^{-2}$	203	203	205
D95	60	$2.7 \times 10^{-3}$	$1.3 \times 10^{-1}$	$7.7 \times 10^{-2}$	$5.2 \times 10^{-1}$	251	252	255

**Supplemental Table 1**

## ADV VELOCITY MEASUREMENTS

Measurements of velocity were made at the channel entrance to ensure that input flow conditions were comparable to shear flows rather than jet flows. In shear flows, the magnitude of the velocity fluctuations in the vertical direction scale to the magnitude of velocity fluctuations in the streamwise direction. A study by Grauss (1971) revealed that the ratio of the standard deviations of velocities in the streamwise direction,  $u'$ , to the vertical direction,  $w'$ , is 3 for shear flows. In our experiments, velocity was sampled with an ADV at the channel entrance in both experiments. The sample volume was located 50 mm above the channel bed and sampled at a frequency of 10 Hz. In the high sinuosity channel experiment, the ratio  $u'/w'$  equaled 3.4, in the low sinuosity channel experiment, the ratio  $u'/w'$  equaled 3.1, while this ratio equaled 3.1 in the straight channel experiments. Values for the ratio  $u'/w'$  close to the value reported by Grauss (1971) support our assumption that flows in our experiment were shear flows driven by buoyancy alone.

The statement that our flows are shear flows is supported by theory presented by Choi and Garcia (2001) to estimate the length of the region of outflow dominated by jet conditions (momentum):

$$(6) \quad l_j = \frac{M_0^{3/4}}{B^{1/2} F_o},$$

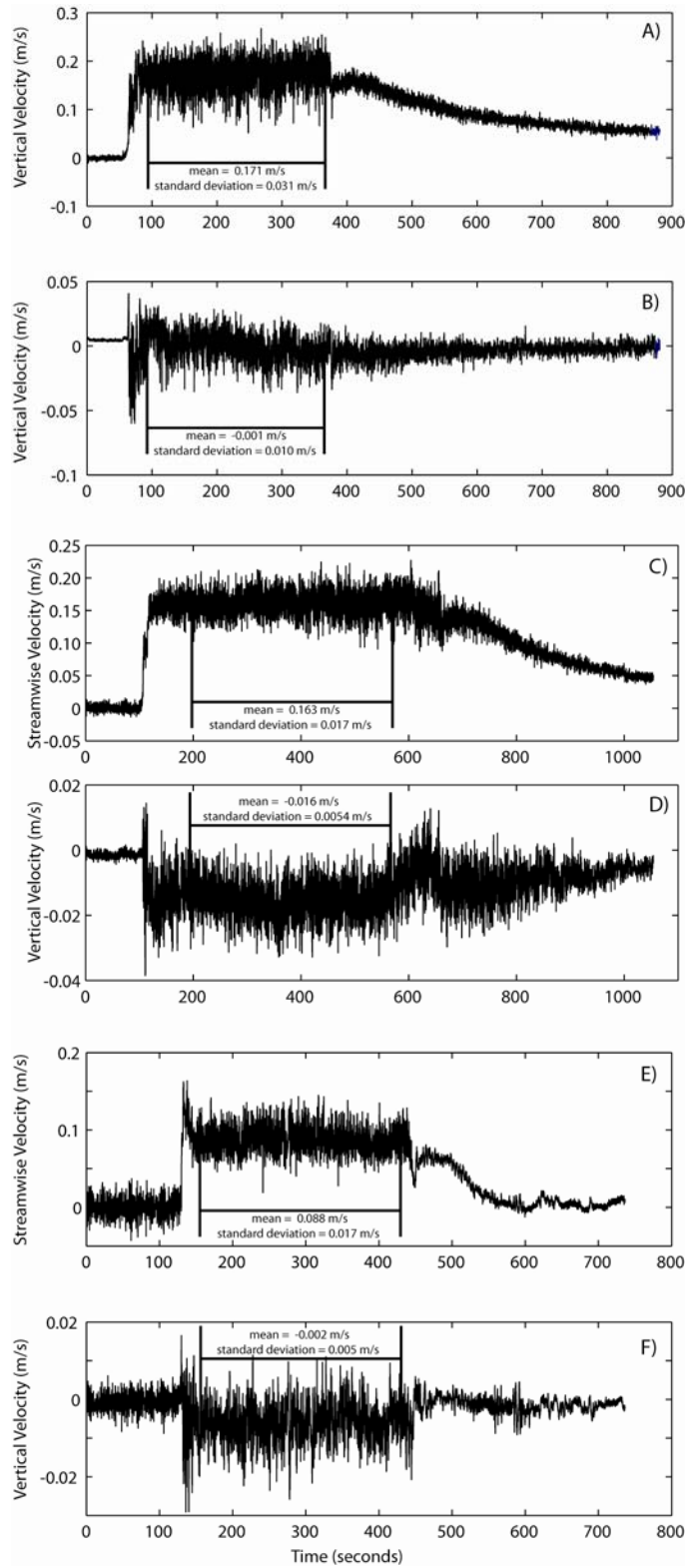
where

$$(7) \quad M_0 = (u^2 hw) + (g' wh^2), \text{ and}$$

$$(8) \quad B_{Fo} = g' uhw$$

with  $u$  being outlet velocity,  $h$  flow thickness, and  $w$  flow width. These equations applied to our experiments give values of 0.21 to 0.28 m downstream from the exit point of our momentum extraction (a short distance relative to the total length of our experimental channels).

Supplemental Figure 5: Time series of velocity measured at the channel entrance, centered over the channel axis, 50 mm above the channel floor. A) Time series of streamwise velocity measured in the straight channel. B) Time series of vertical velocity measured in the straight channel. C) Time series of streamwise velocity measured in the high sinuosity channel. D) Time series of vertical velocity measured in the high sinuosity channel. E) Time series of streamwise velocity measured in the low sinuosity channel. F) Time series of vertical velocity measured in the low sinuosity channel.



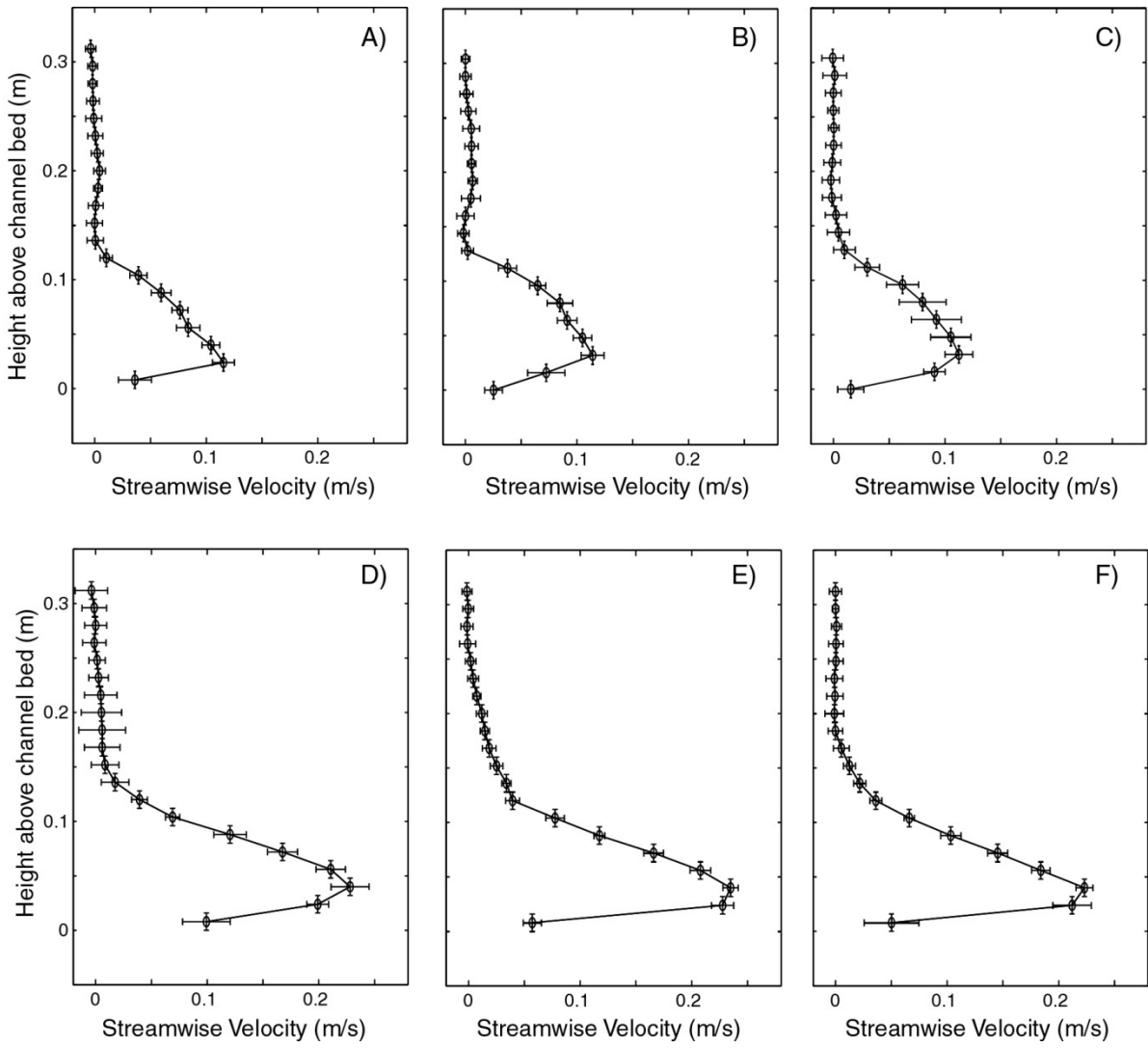
Supplemental Figure 5

## PCADP VELOCITY MEASUREMENTS AND ENTRAINMENT

Profiles of current velocity were measured with a Pulse Coherent Acoustic Doppler Profiler (PCADP) centered over the channel centerline oriented parallel to the channel axis at several distances from the channel entrance in both the straight and sinuous channel experiments. The PCADP measured velocity with a frequency of 0.25 Hz in roughly cylindrical sampling volumes that were  $1.6 \times 10^{-2}$  m deep and had a horizontal footprint that varied in diameter from  $7.1 \times 10^{-2}$  m to  $8.7 \times 10^{-2}$  m with increasing distance from the transducer. Velocity profiles were used to characterize the mean streamwise flow field in each experiment and monitor changes in current thickness. Profiles of current velocity are shown in Supplemental figure 6 at distances from the channel entrance of 1.35, 2.2, and 3.05 m for the high sinuosity channel experiment. These distances correlate to the channel inflection between bends 1 and 2, the apex of bend 2, and the channel inflection between bends 2 and 3. Little change in the structure or thickness of the current with increasing distance from the channel entrance is noted. Profiles of current velocity are shown in Supplemental figure 6 at distances from the channel entrance of 1, 2, and 3 m for the straight channel experiment. Little change in the structure or thickness of the current with increasing distance from the channel entrance is noted.

The bulk Richardson number ( $Ri_B = [gh(\rho_c - \rho_a) / \rho_a] / (\bar{u})^2$ ) is often used to characterize the tendency for mixing of ambient fluid into a current to occur. When  $Ri_B$  is  $\gg 0.25$  velocity shear is not sufficient to overcome the tendency for a stratified flow to remain stratified (Turner, 1973). Inserting characteristic values for  $g$ ,  $h$ ,  $\rho_c$ ,  $\rho_a$ , and  $\bar{u}$  yield  $Ri_B$  of 2.9 and 1.1 for the high sinuosity and straight channel experiments respectively. The high  $Ri_B$  values and minimal change in current thickness with distance from the channel entrance in the two experiments supports minimal entrainment of ambient fluid from above.

Supplemental Figure 6. Profiles of downstream velocity for various currents measured at the channel centerline using the PCADP. Vertical error bars define the extent of each sampling volume while the horizontal error bars are plus and minus one standard deviation calculated using all values for current velocity collected in each sampling volume. A: Velocity profile collected at the channel inflection point between bends 1 and 2, 1.35 m from the sinuous channel entrance. B: Velocity profile collected at the channel bend apex 2, 2.2 m from the sinuous channel entrance. C: Velocity profile collected at the channel inflection point between bends 2 and 3, 3.05 m from the sinuous channel entrance. D: Velocity profile collected 1.0 m from the straight channel entrance. E: Velocity profile collected 2.0 m from the straight channel entrance. F: Velocity profile collected 3.0 m from the straight channel entrance.



**Supplemental Figure 6**

## REFERENCES

- Altinakar, M.S., Graf, W.H., and Hopfinger, E.J., 1996, Flow structure in turbidity currents: *Journal of Hydraulic Research*, v. 34, p. 713-718.
- Bagnold, R.A., 1966, An approach to the sediment transport problem from general physics, U.S. Geological Survey Professional Paper, p. 37.
- Choi, S.-U., and Garcia, M.H., 2001, Spreading of gravity plumes on an incline: *Coastal Engineering Journal*, v. 43, p. 221-237.
- Garcia, M.H., 1994, Depositional turbidity currents laden with poorly sorted sediment: *Journal of Hydraulic Engineering*, v. 120, p. 1240-1263.
- Graf, W.H., 1971, *Hydraulics of sediment transport*: New York, McGraw-Hill, 513 p.
- Grauss, A.J., 1971, Structural features of turbulent flow over smooth and rough boundaries: *Journal of Fluid Mechanics*, v. 50, p. 233-255.
- Nino, Y., Lopez, F., and Garcia, M.H., 2003, Threshold for particle entrainment into suspension: *Sedimentology*, v. 50, p. 247-263.
- Parker, G., Garcia, M.H., Fukushima, Y., and Yu, W., 1987, Experiments on turbidity currents over an erodible bed: *Journal of Hydraulic Research*, v. 25, p. 123-147.
- Parsons, J.D., and Garcia, M.H., 1998, Similarity of gravity current fronts: *Physics of Fluids*, v. 10, p. 3209-3213.
- Pirmez, C., and Imran, J., 2003, Reconstruction of turbidity currents in Amazon Channel: *Marine and Petroleum Geology*, v. 20, p. 823-849.
- Turner, J.S., 1973, *Buoyancy effects in fluids*: Cambridge, U.K., Cambridge University Press, 292 p.